Electronic supplementary information (ESI) for:

Construction of oxygen-bridged multi-interface sites in nanotubes for high-efficiency electrocatalytic nitrite reduction to ammonia

Zhenyong Song,[a,b] Chen Wang,[a,b] Zunhui Xie,[a,b] Chengxiang Liu,[b] Qiqi Zhou,[b] Mingfu Ye,[a,b] Zhanku Li,[b] Fanghui Wu,*[a] Guohong Fan,*[b] and Konglin Wu*[a,b,c]

[a] *Key Laboratory of Metallurgical Emission Reduction & Resources Recycling, Ministry of Education, Anhui University of Technology, Maanshan 243032, P. R. China.*

[b] *Institute of Clean Energy and Advanced Nanocatalysis (iClean), School of Chemistry and Chemical Engineering, Anhui University of Technology, Maanshan 243032, P. R. China.*

[c] *State Key Laboratory of Heavy Oil Processing, China University of Petroleum (East China), Qingdao 266580, P. R. China.*

*Corresponding authors:
E-mails: wfhwfh@ahut.edu.cn (F. Wu);
ghfan8@ahut.edu.cn (G. Fan);
klwuchem@ahut.edu.cn (K. Wu).

Experimental section

Chemicals and materials

$Na^{14}NO_2$, $Na^{15}NO_2$, Na_2SO_4, powdered instant sodium silicate ($Na_2O{\cdot}nSiO_3$, n = 3.1−3.4), maleic acid, ethanol, sulfanilamide, deuterated water (D_2O), sodium citrate, and sodium hypochlorite solution were purchased from Aladdin Industrial Corporation. $Mg(NO_3)_2{\cdot}6H_2O$, $NiCl_2{\cdot}6H_2O$, ammonium chloride (NH_4Cl), sulfuric acid (H_2SO_4), and sodium hydroxide (NaOH) were obtained from Sinopharm Chemical Reagent Co., Ltd. Salicylic acid and Nafion D-520 dispersion (5wt% in water and 1-propanol) were sourced from Macklin Biochemical Co., Ltd.

Synthesis of $(Ni_x,Mg_{1-x})_3Si_2O_5(OH)_4$ with different molar ratio of Ni^{2+} to Mg^{2+}

A solvothermal method was employed to controllably synthesize $(Ni_x,Mg_{1-x})_3Si_2O_5(OH)_4$ nanotubes (named as Ni_1Mg_1SiO NTs, Table S1).[1] The detailed procedure is described as follows: 1.0 mmol $Mg(NO_3)_2{\cdot}6H_2O$ and 1.0 mmol $NiCl_2{\cdot}6H_2O$ were added into 30 mL of deionized H_2O under magnetic stirring for 10 min to obtain a uniform solution. Under vigorous magnetic stirring, 4 mL $Na_2O{\cdot}nSiO_3$ solution was added into the above solution. The reaction system gradually turns into a grey-green suspended slurry. And then, 6 g NaOH solid was added into the above grey-green slurry. Continue stirring for another 10 min to ensure complete dissolution of NaOH. Subsequently, it was transferred to Teflon-lined stainless-steel autoclave (50 mL) and reacted at 200 °C for 24 h. After the reaction was completed, it was naturally cooled to room temperature. The obtained product was centrifuged (2000 rpm) and washed with H_2O and ethanol for 3 times, respectively. Finally, the Ni_1Mg_1SiO NTs were obtained through freeze-drying. In addition, by using the same synthesis process mentioned above and adjusting the molar ratio of Ni^{2+} to Mg^{2+} (Table S1), the $Ni_3Si_2O_5(OH)_4$ nanoparticles (NiSiO NPs), Mg $Mg_3Si_2O_5(OH)_4$ NTs (MgSiO NTs), $(Ni_{0.25},Mg_{0.75})_3Si_2O_5(OH)_4$ NTs (Ni_1Mg_3SiO NTs), and $(Ni_{0.75},Mg_{0.25})_3Si_2O_5(OH)_4$ NTs (Ni_3Mg_1SiO NTs) were obtained, respectively.

Materials characterizations

Structure information and purity of the obtained samples were characterized by an X-ray powder diffractometer (XRD, Rigaku D/max 2500Pc, Cu Kα radiation, λ = 1.5418 Å). The morphology of the obtained samples was characterized by transmission electron microscopy (TEM, Hitachi H-7700/7800, working voltage 100 kV). High-resolution TEM (HRTEM) image and high-angle annular dark-field scanning transmission electron microscopy (HAADF-STEM) image were carried out on the Thermo Scientific Talos 200S (working voltage 200 kV). Elemental mapping images were obtained from the energy-dispersive X-ray spectroscopy (EDS) installed on the Thermo Scientific Talos 200S (working voltage 200 kV).

X-ray photoelectron spectroscopy (XPS) was obtained on a Thermo Scientific K-Alpha instrument (Mono AlKa, working voltage 12 kV, beam current 6 mA). The N_2 adsorption-desorption isotherm experiment was measured by the fully automatic specific surface area and pore size analyzer (ASAP 2460, Micromeritics). The oxygen vacancies in the samples were tested by using electron paramagnetic resonance (EPR) spectroscopy (EMXplus, Bruker). The quantitative determination of the products in the electrocatalytic reduction of NO_2^- to NH_3 is carried out using an ultraviolet-visible spectrophotometer (UV-3600i Plus, Shimadzu). The qualitative and quantitative determination of NH_3 were characterized by nuclear magnetic resonance hydrogen spectroscopy (^{1}H-NMR, Bruker AVANCE 400). Qualitative analysis of the gaseous products was carried out by gas chromatography (GC, GC-2014, Shimadzu). *In-situ* attenuated total reflection-Fourier Transform infrared spectroscopy (ATR-FTIR, Bruker Vertex 70 V/s FTIR spectrometer) and *In-situ* Raman spectroscopy (inVia, Renishaw, excitation wavelength 532 nm) were employed to detect the intermediates during the electrocatalytic reduction of NO_2^-. Inductively coupled plasma (ICP) emission spectrometer (ICP-7510, Shimadzu) is used to detect the concentration of metal ions in the electrolyte.

Electrochemical performances

All electrochemical measurements were conducted using a CHI 760E electrochemical workstation (Shanghai Chenhua Instrument Co., Ltd.) via a three-electrode system in a typical H-type cell separated by a membrane (Nafion XL, Dupont). The catalyst deposited on carbon paper (1.0 × 1.0 cm^2) as working electrode, saturated Ag/AgCl electrode as reference electrode, and Pt wire as counter electrode, respectively. Electrochemical experiments were conducted in Ar-saturated 0.5 M Na_2SO_4 solution (30 mL), both without and with added $NaNO_2$ (0.5 M). In this work, all electrochemical data were calculated relative to the reversible hydrogen electrode (RHE) using the following equation: $E_{(RHE)} = E_{(Ag/AgCl)} + 0.197\ V + 0.059 \times pH$. The working electrode was prepared as follows: 10 mg of catalyst was dispersed in a mixed solution comprising 500 μL ethanol, 450 μL ultrapure water, and 50 μL Nafion D-520 dispersion. The mixture was sonicated for 1 h to form a uniform catalyst ink. And then, 100 μL catalyst ink was dropped onto the surface of carbon paper (1.0 × 1.0 cm^2) and dried to obtain the working electrode. The loading of the catalyst was 1 mg cm^{-2}. The electrocatalytic NO_2RR performance was conducted in Ar-saturated neutral electrolyte (30 mL solution containing 0.5 M Na_2SO_4 and 0.5 M $NaNO_2$). First, the electrode activation was achieved through cyclic voltammetry (scan rate 10 mV s^{-1}, potential range −1.2 to 0.4 V vs. RHE). At different potentials, the enrichment experiments were carried out by chronopotentiometry (i-t), and then the NH_3 yield rate and Faraday efficiency (FE) of the different catalysts were obtained by colorimetry.[2]

Determination of NH_3

Determine the generated NH_3 using the indophenol blue spectrophotometric (IBS) method.[2–4] Typically, 1 mL of the solution after electrocatalysis and dilute it to 5 mL with deionized water. Then, add 2 mL of 1.0 M NaOH containing 5 wt% H_2SO_4 and 5 wt% sodium citrate, followed by 1 mL of 0.05 M NaClO solution and 0.2 mL of 1 wt% sodium nitroferrocyanide. After standing at room temperature for 2 h, collect the UV-visible absorption spectrum at a wavelength of 655 nm. Calibrate the concentration-absorbance curves using a series of standard NH_4Cl solutions (**Fig. S10**).

Isotope Labeling Experiments by ^{1}H-NMR.

The ammonia ($^{14}NH_4^+$ and $^{15}NH_4^+$) yield rate after electrolysis was quantified by the ^{1}H-NMR spectroscopy.[2, 3] The calibration curves with defined $^{15}NH_4Cl$ (abundance of ^{15}N species: ⩾99 atom%) concentrations were constructed as standards, Maleic acid ($C_4H_4O_4$) was used as an external standard. In a typical procedure, adding hydrochloric acid (0.1 M) to 0.9 mL of standard solution/electroltes to adjust the pH of the solution to 2. Next, the solution was mixed with 0.1 mL of deuterium oxide (D_2O) containing maleic acid. Finally, the prepared solution was tested by a 400 MHz NMR spectrometer using the water suppression method.

Calculation of yield, selectivity, and Faraday efficiency (FE)

The following formula converts the potential (relative to saturated Ag/AgCl) to RHE[2–4]:

$$E_{\mathrm{RHE}} = E_{\mathrm{Ag/AgCl}} + 0.059 \times \mathrm{pH} + E^{\theta}_{Ag/AgCl}$$

Formula for calculation： $\mathrm{FE} = (\mathrm{N} \times \mathrm{F} \times \mathrm{C} \times \mathrm{V}) / (\mathrm{M} \times \mathrm{Q})$

Here, N denotes the number of electron transfers required to form 1 mol of the product, with NH_3 being 8; F is the Faraday constant, equal to 96485 C mol^{-1}; C represents the product concentration; V is the volume of the cathode compartment electrolyte; M denotes the relative molecular mass, with NH_3 being 17 g mol^{-1} and NO_2^- being 46 g mol^{-1}; Q is the charge quantity during 30 min of electrolysis. The NH_3 yield at a specific applied potential is calculated using the following equation:

$$NH_3 \text{ yield} = (C_{NH3} \times V) / (S_{cat} \times t)\ \mu mol\ h^{-1}\ cm^{-2}$$

Scat represents the loading area of the catalyst; t represents the duration of electrolyte electrolysis.

***In-situ* Raman testing**

The experiment was conducted using an improved electrochemical Raman cell (a three-electrode polyvinylidene fluoride-based cell with a 0.5 mm thick sapphire window) and a confocal Raman spectrometer (inVia, Renishaw). A 532 nm excitation laser (50 mW, 10% output energy) was used as the light source, with a grating of 1800, and focused on the sample surface through a 50X long-focal-length objective lens. During the Raman measurement, the

distance between the sapphire window and the surface of the working electrode was less than 0.1 mm, which made the solution layer on the surface of the working electrode very thin, thus minimizing the attenuation effect of the solution layer on the Raman signal. Ni_1Mg_1SiO NTs was used as the catalyst, and its *In-situ* Raman spectra at different potentials (vs. RHE) and at constant potential (-0.79 V vs. RHE) for different times were detected.

Calculation details

The density functional theory (DFT) calculations were performed with the Vienna Ab Initio Simulation Package (VASP)[5, 6]. Spin polarized DFT calculations were adopted for all the calculations. The interaction between ionic cores and valence electrons was described using the projector augmented plane-wave (PAW) method[7, 8] The Perdew-Burke-Ernzerhof (PBE) exchange-correlation functional within the generalized gradient approximation (GGA) was employed for exchange-correlation effects on the total energies[9]. The effect of van der Waals interaction was described using the dispersion-corrected DFT-D3 functional[10]. A vacuum of 15 Å was added along the z-direction to avoid the effects from nearby slabs. The convergence thresholds for force and energy were 0.05 eV $Å^{-1}$ and 1×10^{-5} eV/atom respectively. The energy cutoff for the plane-wave basis was set to 450 eV. The $2 \times 2 \times 1$ k-point grid was used to sample the Brillouin zone for geometry optimization, and a $6 \times 6 \times 1$ k-point grid was used for electronic structure calculation such as density of states.

The Gibbs free energy is determined by the equation:

$$G = E_{DFT} + E_{ZPE} - TS \qquad (S1)$$

where E_{DFT} and E_{ZPE} are the total energy and zero-point energy calculated with VASP, TS is the entropy contribution at 298.15 K. The free energy change of each step that involves the electrochemical proton-electron transfer was described by the computational hydrogen electrode (CHE) model proposed by Nørskov et al[11].

To avoid the calculation of the charged NO_2^- species within the periodic DFT calculations, we used neutral gas-phase HNO_2 as reference instead[12]. The energy for the nitrate ion was obtained by using reference values for the ionization energy of H and the heat of reaction for HNO_2 (g) deprotonation[13].

The adsorption energy (ΔE_{ads}) of reactants or intermediates on the catalyst surface was defined as: $\Delta E_{ads} = E_{total} - E_{slab} - E_{ads}$, where E_{total} represents the total energy of slab with the adsorbate, E_{slab} represents the energy of isolated slab, and E_{ads} represents the energy of the adsorbate in gas phase.

References:

(1) W. Zhu, Y. Yang, S. Hu, G. Xiang, B. Xu, J. Zhuang, X. Wang, *Inorg. Chem.*, 2012, ***51***,

6020−6031.

(2) C. Peng, M. Wang, S. Li, X. Zeng, J. Wang, W. Wang, Z. Zhang, M. Ye, X. Wei, K. Wu, K. Zhang, J. Zeng, *Angew. Chem. Int. Ed.*, 2024, ***63***, e202408771.

(3) K. Yao, Z. Fang, W. Yan, Y. Wang, Z. Song, W. Wang, J. Wang, X. Wei, Y. Tan, D. Wu, K. Wu, B. Jiang, *Chem. Commun.*, 2024, ***60***, 2756–2759.

(4) Z. Chen, Y. Zhao, H. Huang, G. Liu, H. Zhang, Y. Yan, H. Li, L. Liu, M. Liu, D. Wang, J. Zeng, *J. Am. Chem. Soc.*, 2025, *147*, 18737−18746.

(5) G. Kresse, J. Furthmüller, *Comput. Mater. Sc.*, 1996, ***6***, 15–50.

(6) G. Kresse, J. Furthmüller, *Phys. Rev. B*, 1996, ***54***, 11169–11186.

(7) P. E. Blöchl, *Phys. Review B*, 1994, ***50***, 17953–17979.

(8) G. Kresse, D. Joubert, *Phys. Rev. B*, 1999, ***59***, 1758–1775.

(9) J. P. Perdew, K. Burke, M. Ernzerhof, *Phys. Rev. Lett.*, 1996, ***77***, 3865–3868.

(10) S. Grimme, J. Antony, S. Ehrlich, H. Krieg, *J. Chem. Phys.*, 2010, ***132***, 154104.

(11) J. K. Nørskov, J. Rossmeisl, A. Logadottir, L. Lindqvist, J. R. Kitchin, T. Bligaard, H. Jónsson, *J. Phys. Chem. B*, 2004, ***108***, 17886–17892.

(12) S. Guo, K. Heck, S. Kasiraju, H. Qian, Z. Zhao, L. C. Grabow, J. T. Miller, M. S. Wong, *ACS Catal.*, 2018, ***8***, 503–515.

(13) W. A. Chupka, J. Berkowitz, D. Gutman, *J. Chem. Phys.*, 1971, ***55***, 2724–2733.

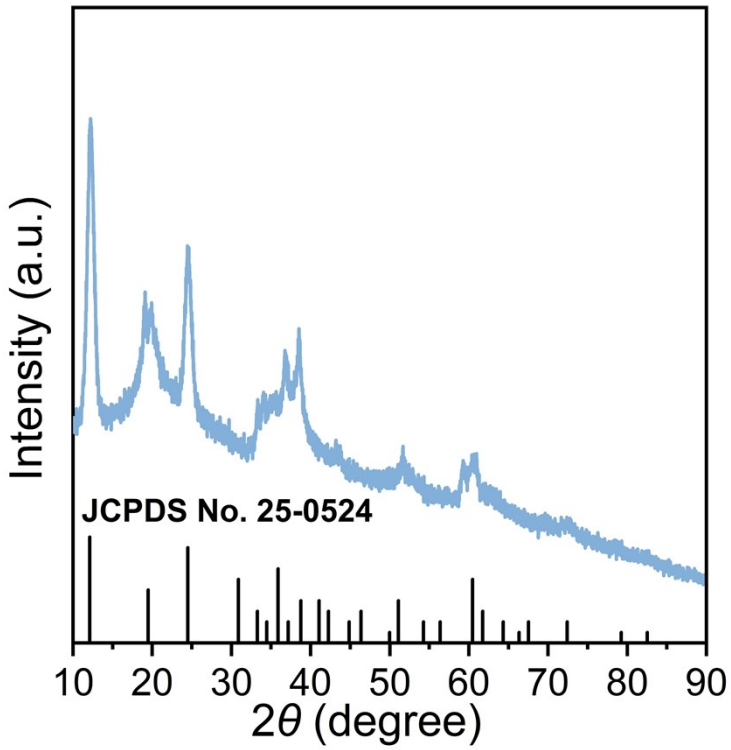

Fig. S1 XRD pattern of Ni_1Mg_1SiO NTs.

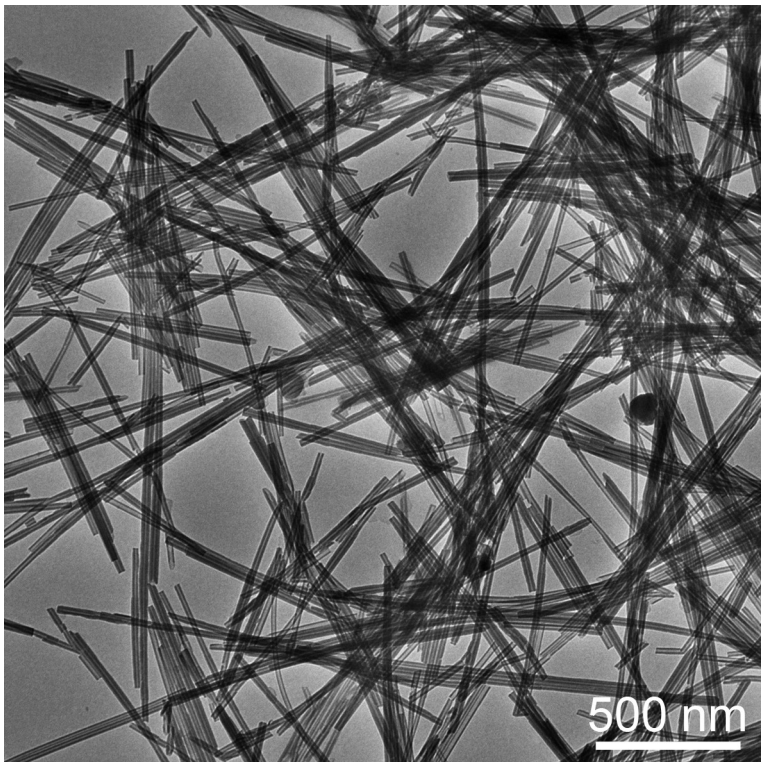

Fig. S2 Low-resolution TEM image of Ni_1Mg_1SiO NTs.

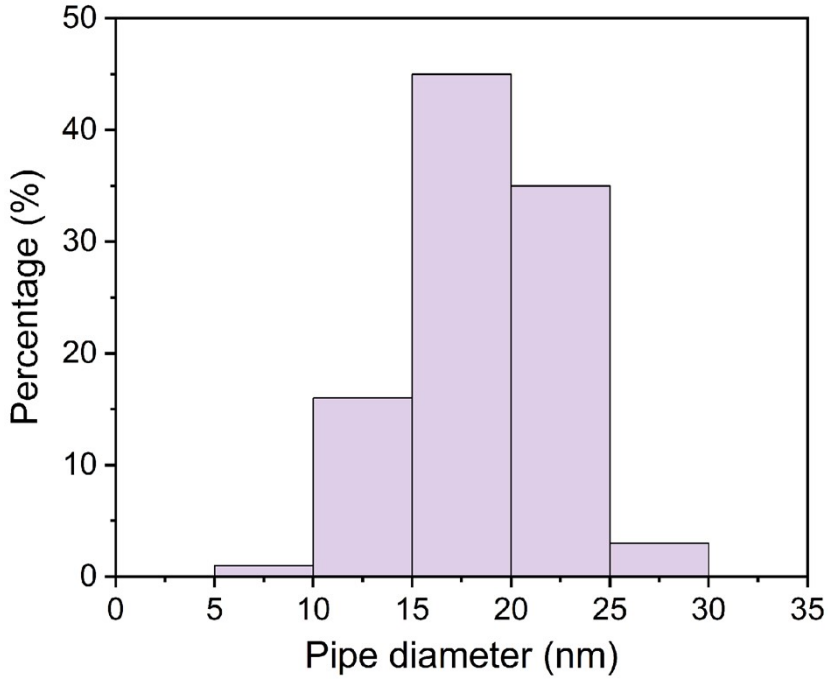

Fig. S3 The tube diameter distribution of Ni_1Mg_1SiO NTs.

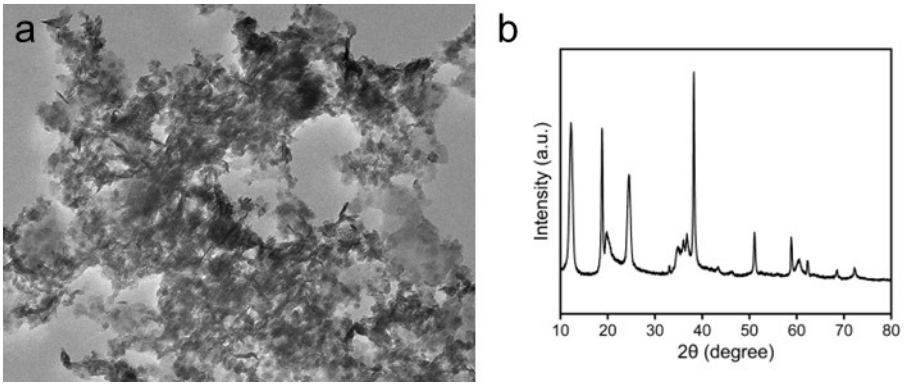

Fig. S4 TEM image and (b) XRD pattern of NiSiO NPs.

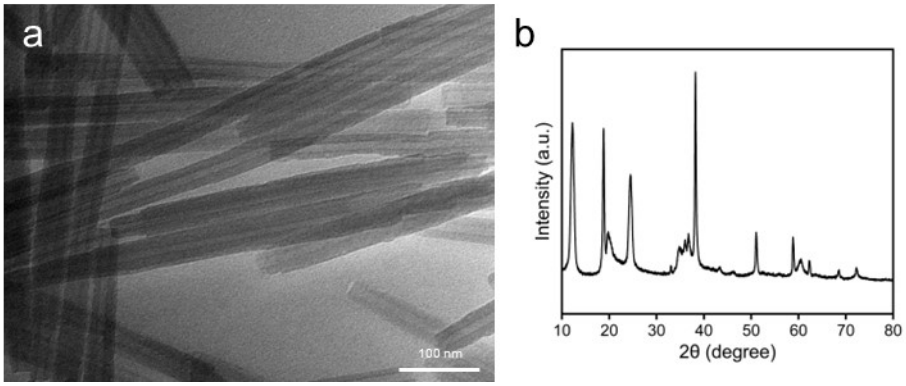

Fig. S5 TEM image and (b) XRD pattern of MgSiO NTs.

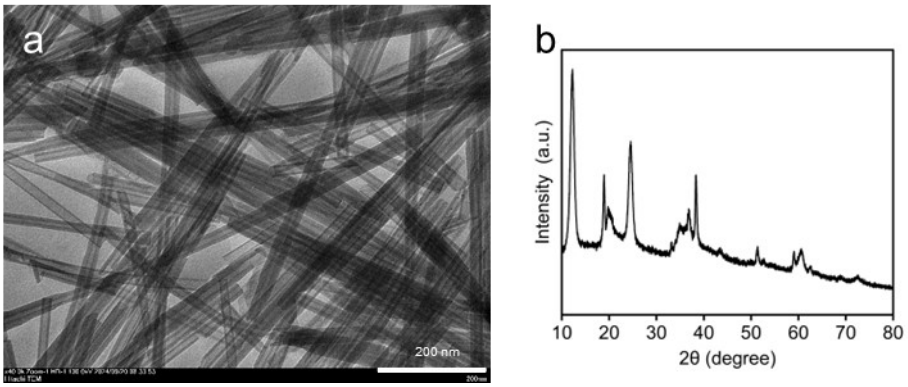

Fig. S6 TEM image and (b) XRD pattern of Ni_1Mg_3SiO NTs.

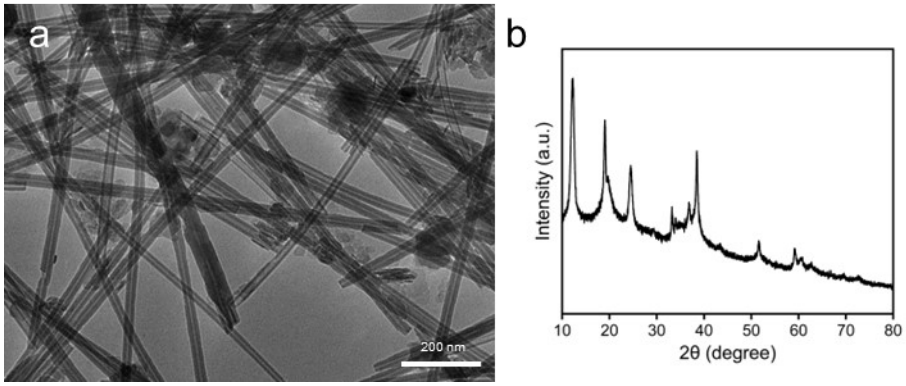

Fig. S7 TEM image and (b) XRD pattern of Ni_3Mg_1SO NTs.

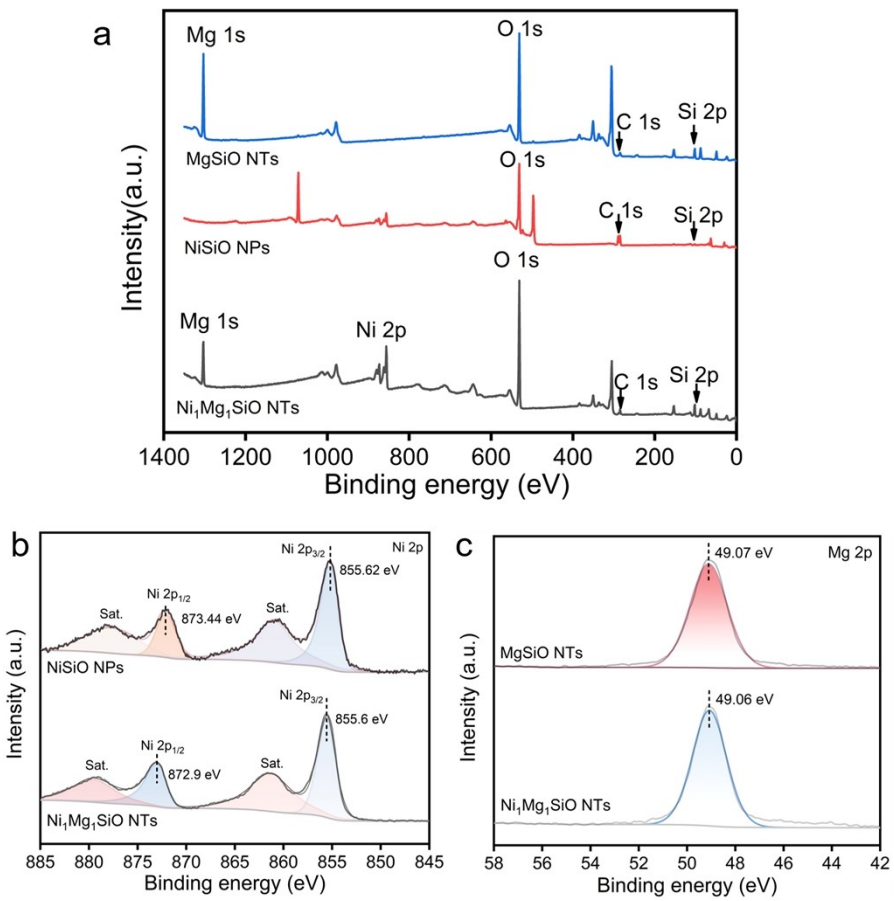

Fig. S8 (a) The survey XPS spectra of Ni_1Mg_1SiO NTs, NiSiO NPs and MgSiO NTs. (b) High resolution Ni 2p XPS spectra of Ni_1Mg_1SiO NTs and NiSiO NPs. (c) High resolution Mg 2p XPS spectra of Ni_1Mg_1SiO NTs and MgSiO NTs.

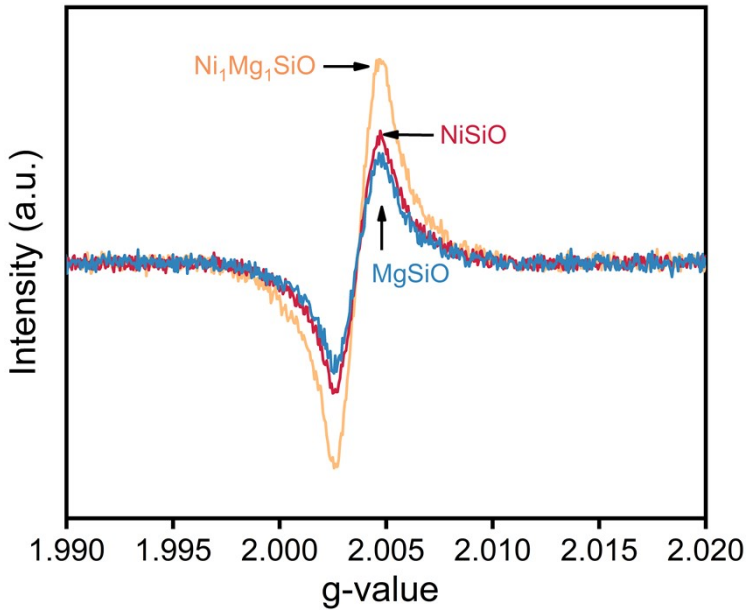

Fig. S9 Electron paramagnetic resonance spectra of Ni_1Mg_1SiO NTs, NiSiO NPs, and MgSiO NTs.

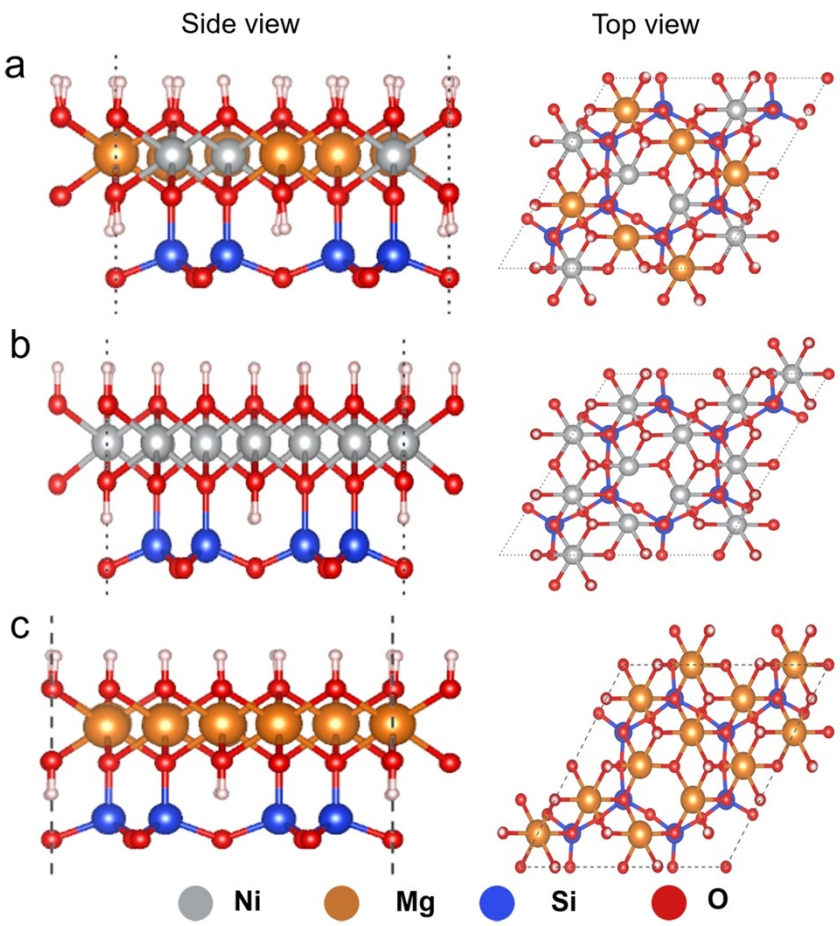

Fig. S10 Structural models of three different catalysts (side view and top view). (a) Ni_1Mg_1SiO NTs, (b) NiSiO NPs, and (c) MgSiO NTs.

As shown in Fig. S10, the structural models of the above three different catalysts (Ni_1Mg_1SiO NTs, Ni_1SiO NPs, and Mg_1SiO NTs) were given by combining experiments and SpringerMaterials database (https://materials.springer.com/isp/crystallographic/docs/sd_1225403). Slab models of MgSiO NTs, Ni_1Mg_1SiO NTs, and NiSiO NPs with vacancy was constructed (Fig. S9). Slab models of Ni_1Mg_1SiO NTs was built by replacing one-half of the Mg atoms in the corresponding MgSiO NTs slab model, based on the evidence from the previous characterization results.

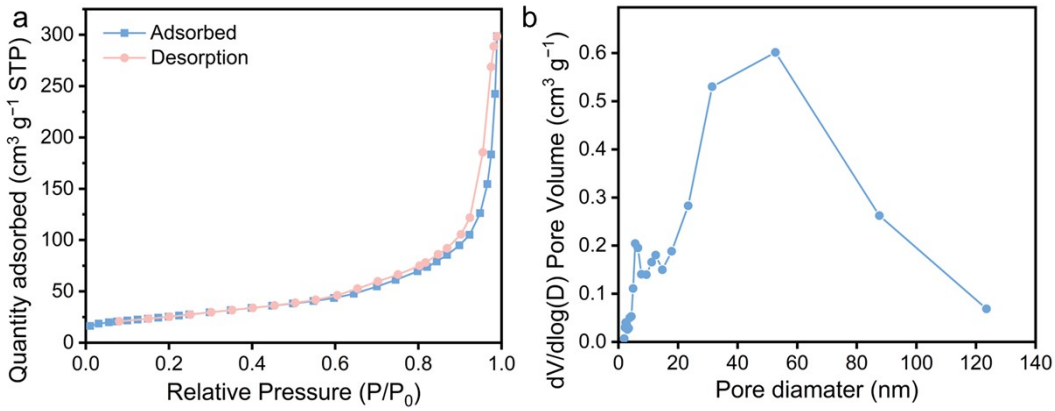

Fig. S11 N_2 isothermal adsorption-desorption curves and corresponding pore size distribution of Ni_1Mg_1SiO NTs.

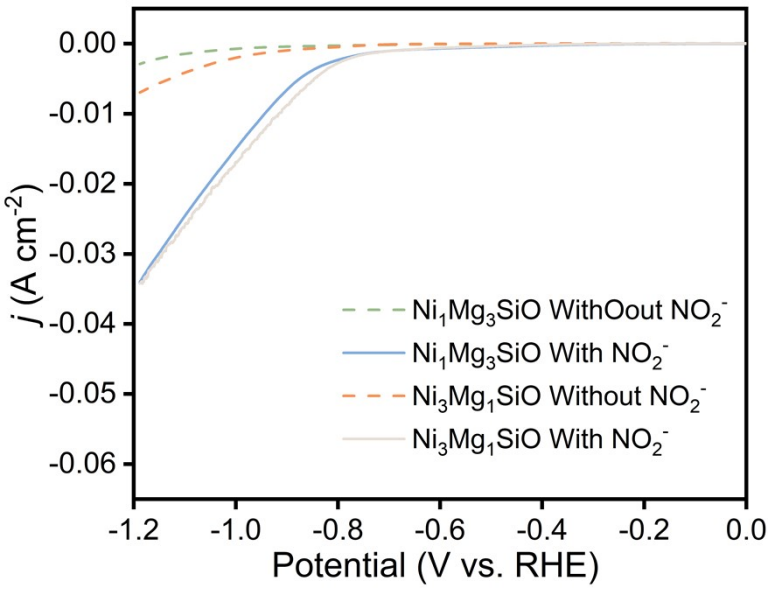

Fig. S12 The LSV curves of Ni_1Mg_3SiO and Ni_3Mg_1SiO NTs in the presence (solid lines) and absence (dash line) of 0.5 M $NaNO_2$ in 0.5 M Na_2SO_4 solution.

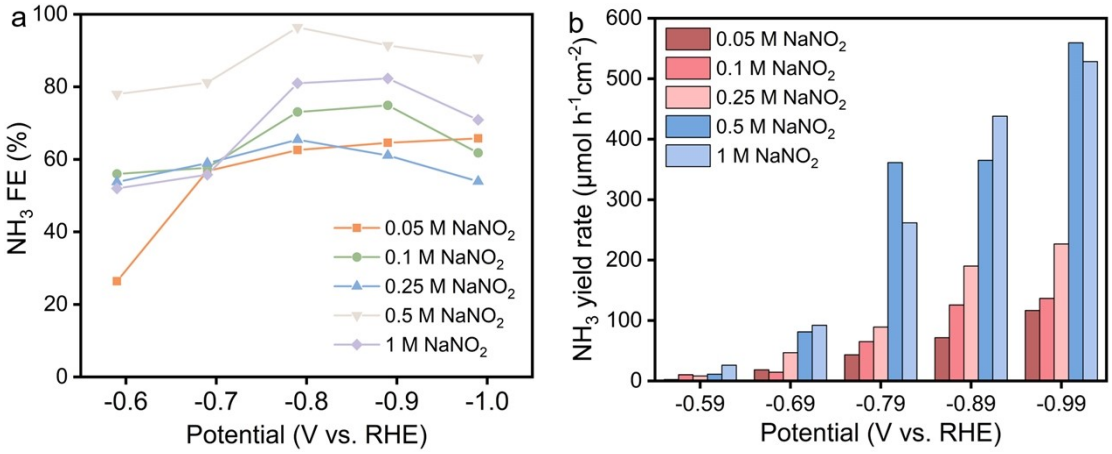

Fig. S13 The NH_3 FEs (a) and (b) NH_3 yield rates of Ni_1Mg_1SiO NTs as catalysts under different potentials in Ar-saturated 0.5 M Na_2SO_4 solution with different concentration of $NaNO_2$ (0.05, 0.1, 0.25, 0.5, and 1 M, respectively).

As shown in Fig. S13, the influence of different $NaNO_2$ concentrations (0.05, 0.1, 0.25, 0.5, and 1 M, respectively) on electrocatalytic NO_2RR activity was investigated. With the increase of $NaNO_2$ concentration, the NH_3 yield rate at different potentials also increased, while the FE first rose and then dropped. Especially in the presence of 0.5 M $NaNO_2$, the Ni_1Mg_1SiO NTs catalysts exhibit the best catalytic activity, with the FE of NH_3 production reaching up to 96.4% and the maximum NH_3 yield rate reaching 559.6 μmol h^{-1} cm^{-2}. Therefore, 0.5 M $NaNO_2$ was selected the optimal concentration.

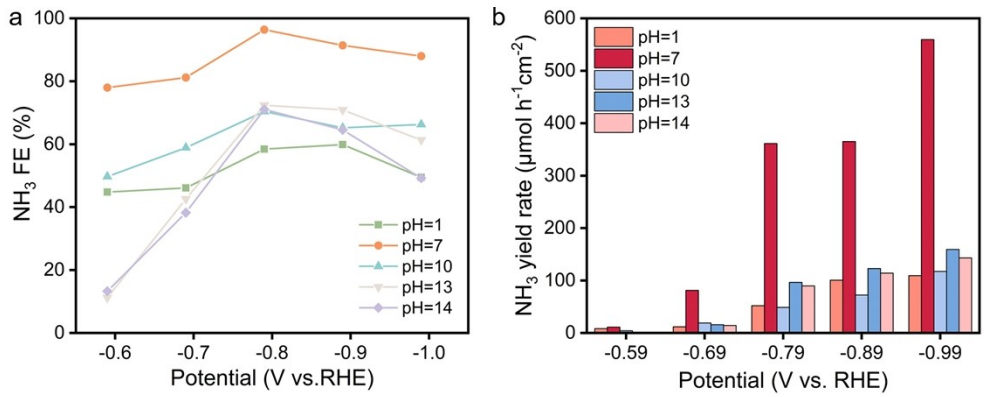

Fig. S14 The NH_3 FEs (a) and (b) NH_3 yield rates of Ni_1Mg_1SiO NTs as catalysts under different potentials in Ar-saturated 0.5 M Na_2SO_4 solution with different pH values (pH = 1, 7, 10, 13, and 14, respectively).

As shown in Fig. S14, the influence of different pH values (pH = 1, 7, 10, 13, and 14, respectively) on electrocatalytic NO_2RR activity was investigated. Both too high and too low pH values were unfavorable for NH_3 synthesis, such as the FEs were lower than 75%, and the NH_3 yield rates were lower than 100 μmol h^{-1} cm^{-2}. The above results indicate that the Ni_1Mg_1SiO NTs catalyst has the highest catalytic activity only when the pH was 7.

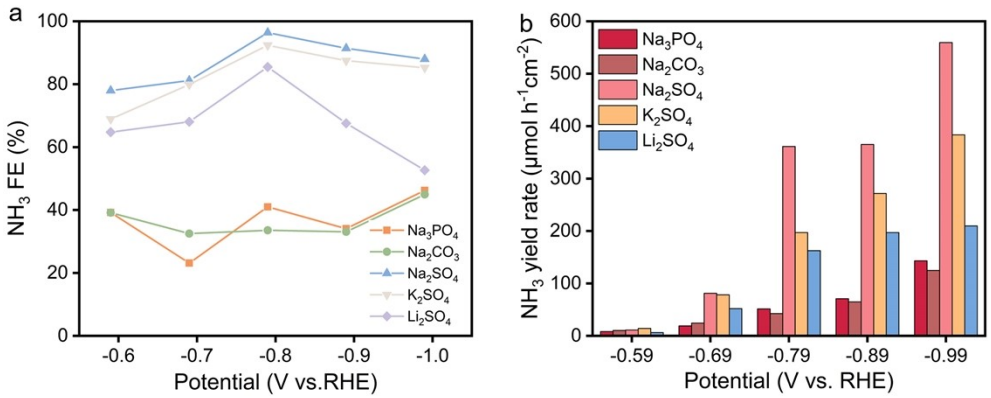

Fig. S15 The NH_3 FEs (a) and (b) NH_3 yield rates of Ni_1Mg_1SiO NTs as catalysts under different potentials in Ar-saturated different electrolytes (0.5 M Na_3PO_4, Na_2CO_3, Na_2SO_4, K_2SO_4, and Li_2SO_4 solution, respectively) with 0.5 M $NaNO_2$.

As shown in Fig. S15, the influence of different electrolytes on electrocatalytic NO_2RR activity was carried out. Different types of cations and anions were selected for the electrolyte types. For instance, Na_3PO_4, Na_2CO_3; K_2SO_4, Li_2SO_4, etc. are used as electrolytes. It can be seen that in Na_3PO_4 and Na_2CO_3, the FEs and NH_3 yield rates are generally low. This indicates that the alkaline environment caused by this type of strong base and weak acid salt is not conducive to the reduction of NO_2^-, which is consistent with the above conclusion that pH value affects catalytic activity (Fig. S15). When Li_2SO_4, Na_2SO_4 and K_2SO_4 are selected as electrolytes, it is obvious that their catalytic activities are all relatively good. Relatively speaking, when Na_2SO_4 is chosen as the electrolyte, it shows the best catalytic activity.

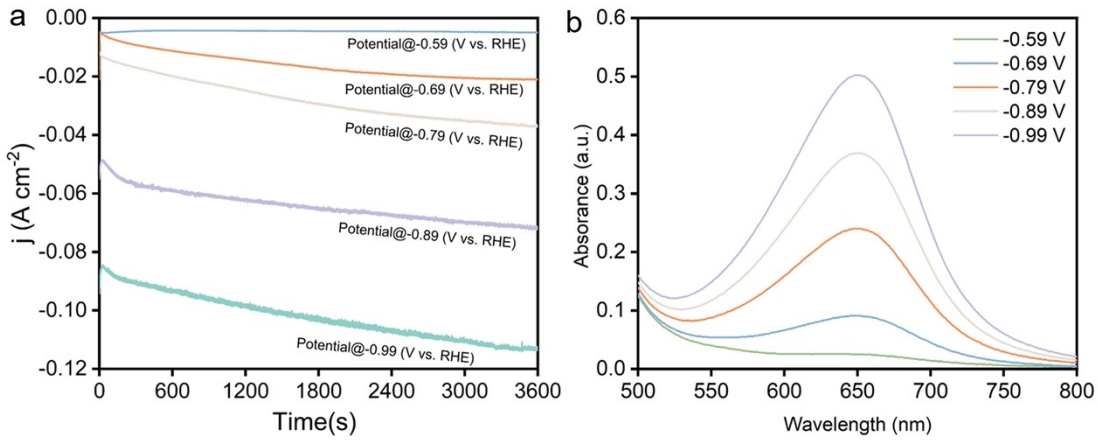

Fig. S16 The (a) i-t curves and (b) UV-vis spectra of electrocatalytic NO_2RR to NH_3 by Ni_1Mg_1SiO NTs as catalyst under different potentials.

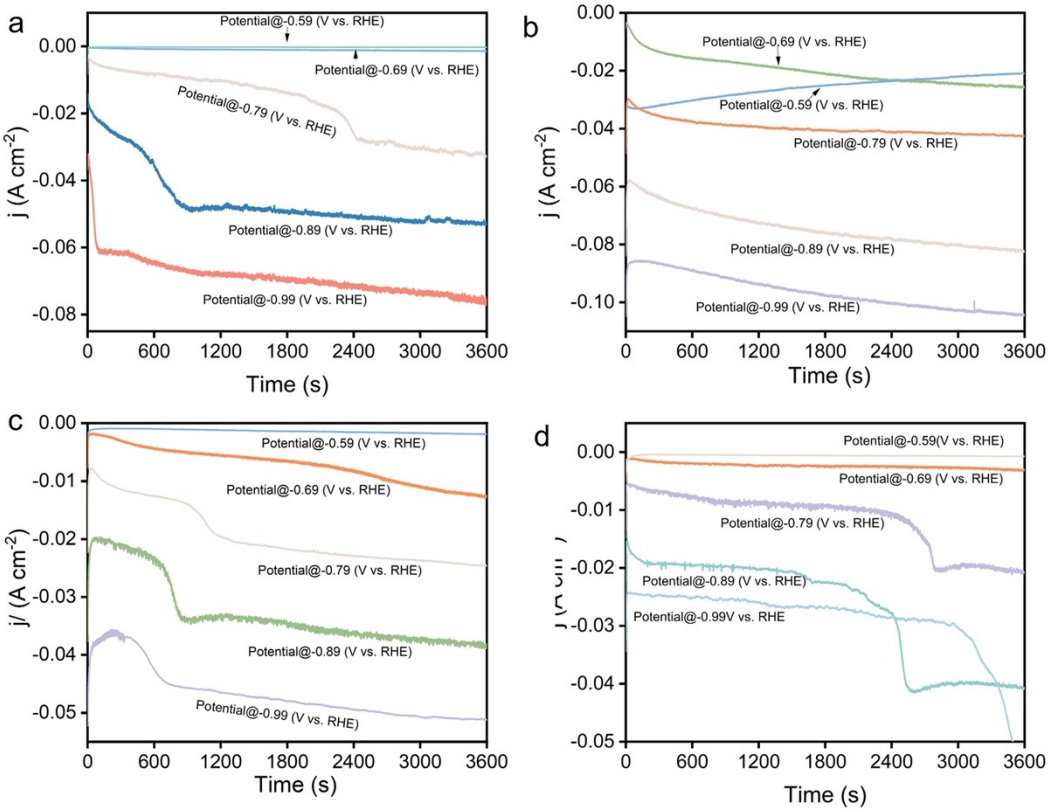

Fig. S17 The i-t curves of electrocatalytic NO_2RR to NH_3 by Ni_3Mg_1SiO NTs, Ni_1Mg_3SiO NTs, MgSiO NTs, and NiSiO NPs as catalyst under different potentials, respectively.

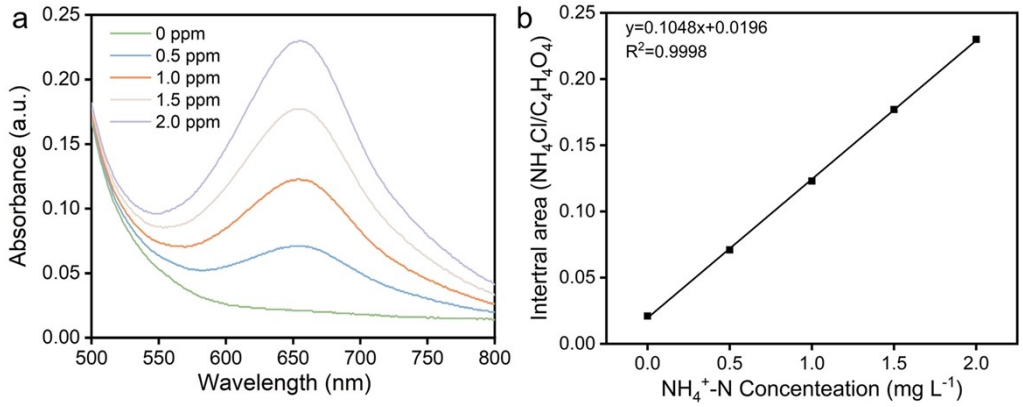

Fig. S18 (a) The UV-vis absorption spectra of NH_4Cl solutions with different concentrations and (b) corresponding standard calibration curve for the determination of NH_3.

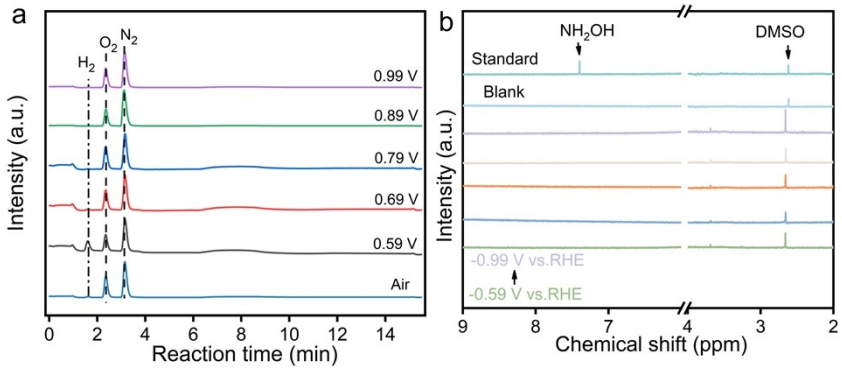

Fig. S19 (a) Analysis of gaseous products and corresponding (b) liquid products of NH_2OH at different potentials (vs. RHE).

As shown in Fig. S19a, gas chromatography analysis shows that only at low potentials is there a significant production of H_2, while at high potentials, no obvious H_2 is produced. The N_2 and O_2 detected mainly comes from the air. NMR (Fig. S19b) detection of hydroxylamine indicates that no significant hydroxylamine is present at different potentials. These results fully demonstrate that the main product of the electrocatalytic reduction of nitrite by this catalyst is ammonia, which proves the high selectivity of the catalyst.

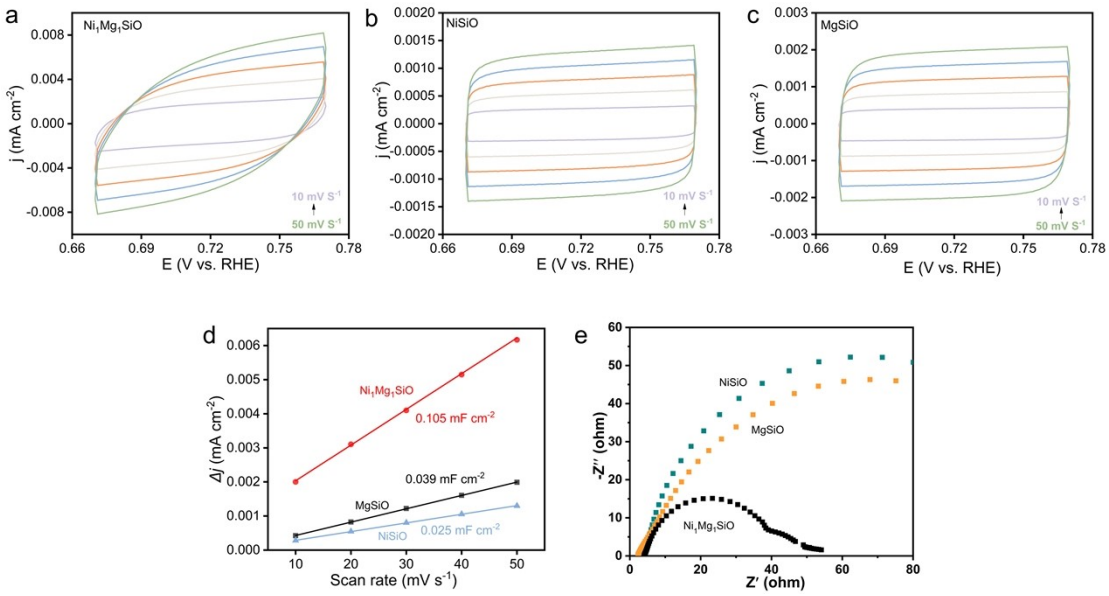

Fig. S20 CV curves of (a) Ni_1Mg_1SiO NTs, (b) MgSiO NTs, and (c) NiSiO NPs. (d) C_{dl} values and (e) Nyquist plots of Ni_1Mg_1SiO NTs, MgSiO NTs, and NiSiO NPs.

As shown in Fig. S20, the source of the activity differences among the three catalysts was investigated through electrochemically active surface area (ECSA) and electrochemical impedance spectroscopy (EIS). Based on the recorded cyclic voltammetry (CV) curves (Figs. S20a−S20c), the ECSA values (Fig. S20d) were obtained for Ni_1Mg_1SiO NTs, MgSiO NTs, and NiSiO NPs. The Ni_1Mg_1SiO NTs (0.105 mF cm^{-2}) owns the largest ECSA in conjunction with MgSiO NTs (0.039 mF cm^{-2}) and NiSiO NPs (0.025 mF cm^{-2}), respectively. This result indicates that Ni_1Mg_1SiO NTs have more active sites than other catalysts. The further EIS results (Fig. S20e) displayed that the Ni_1Mg_1SiO NTs show a smaller impedance indicates that it is more conducive to the transmission of electrons. The above results further prove that Ni_1Mg_1SiO NTs have more excellent catalytic activity.

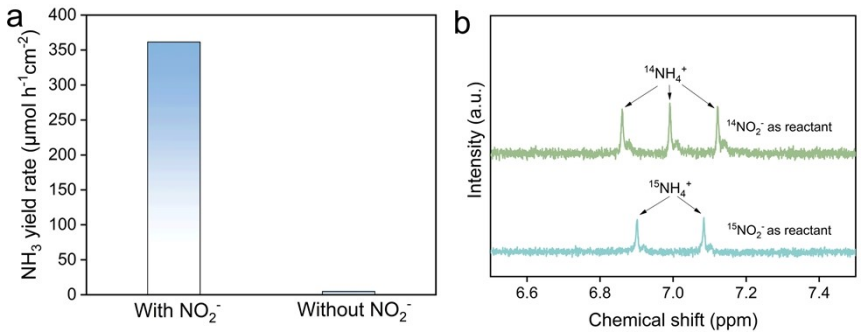

Fig. S21 (a) NH_3 yield rate for Ni_1Mg_1SiO NTs as the catalyst at 0.5 M Na_2SO_4 electrolyte with or without 0.5 M $NaNO_2$ at −0.79 V vs RHE. (b) ^{1}H-NMR spectra for Ni_1Mg_1SiO NTs as catalyst for NH_3 synthesis in Ar-saturated 0.5 M Na_2SO_4 with $Na^{14}NO_2$ and $Na^{15}NO_2$.

To verify that the NH_3 detected in the product originated from NO_2^- in the solution, a constant potential method was employed using 0.5 M Na_2SO_4 electrolyte in the absence and presence of 0.5 M $NaNO_2$ at −0.79 V vs RHE (Fig. S21a). The analysis of the electrolysis products indicated that almost no NH_3 was detected in the absence of 0.5 M $NaNO_2$ (Fig. S21a), suggesting that there were no amino contaminants in the reagents and chemicals utilized during the testing process. Upon introducing 0.5 M $NaNO_2$, a significant amount of NH_3 was detected, providing preliminary evidence that the NH_3 in the product indeed originated from NO_2^- (Fig. S21a). Furthermore, an ^{15}N isotope labeling experiment was performed to further substantiate these findings, and the N source in the synthesized NH_3 was confirmed by ^{1}H-NMR spectroscopy (Fig. S21b). When $Na^{15}NO_2$ and $Na^{14}NO_2$ were used as electrolytes, two distinct characteristic peaks corresponding to $^{15}NH_4^+$ and three distinct characteristic peaks corresponding to $^{14}NH_4^+$ were observed, respectively, which further corroborated that the generated NH_3 originated from the reduction of NO_2^-. Leveraging the direct proportional relationship between peak area and NH_4^+ content in the ^{1}H-NMR spectrum, a quantitative analysis of the generated NH_3 was carried out using maleic acid as an internal standard (Fig. S22). The measured yields of both $^{15}NH_4^+$ and $^{14}NH_4^+$ closely aligned with those obtained via IBS (Fig. S23). This not only verifies the accuracy and reliability of our colorimetric approach but also reinforces our conclusion that generated NH_3 primarily arises from the NO_2RR rather than contamination by external N sources.

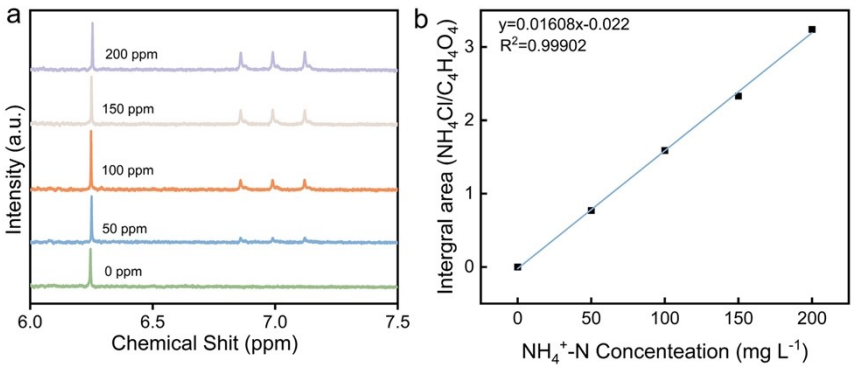

Fig. S22 (a) ^{1}H NMR spectra of the standard $^{14}NH_4^+$ solutions with different concentrations and (b) corresponding standard curve of integral area ($^{14}NH_4^+$-$^{14}N/C_4H_4O_4$) against $^{14}NH_4^+$-^{14}N concentration.

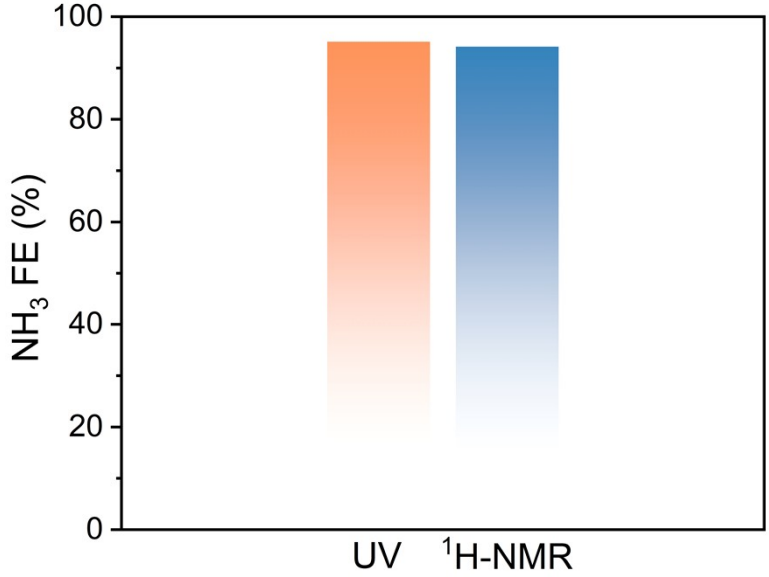

Fig. S23 The FEs of electrocatalytic NO_2RR to NH_3 were calculated using the UV-vis absorption spectroscopy and ^{1}H-NMR spectroscopy technology by using Ni_1Mg_1SiO NTs as the catalyst.

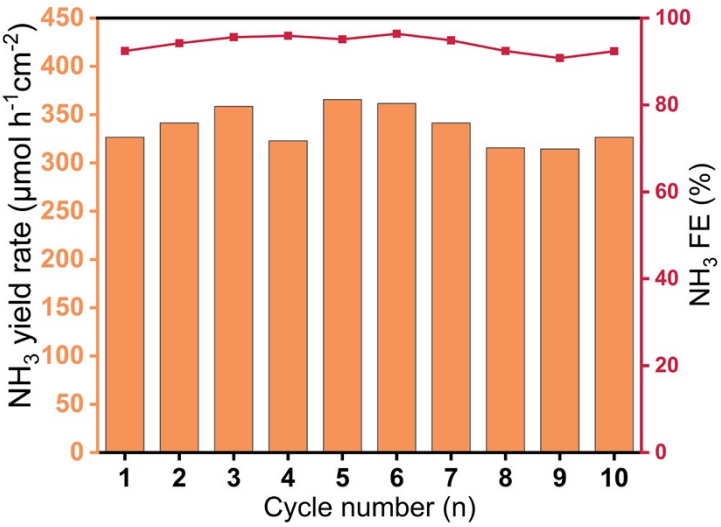

Fig. S24 Cycling test of Ni_1Mg_1SiO NTs at −0.79 V vs. RHE for 60 min in H-cell.

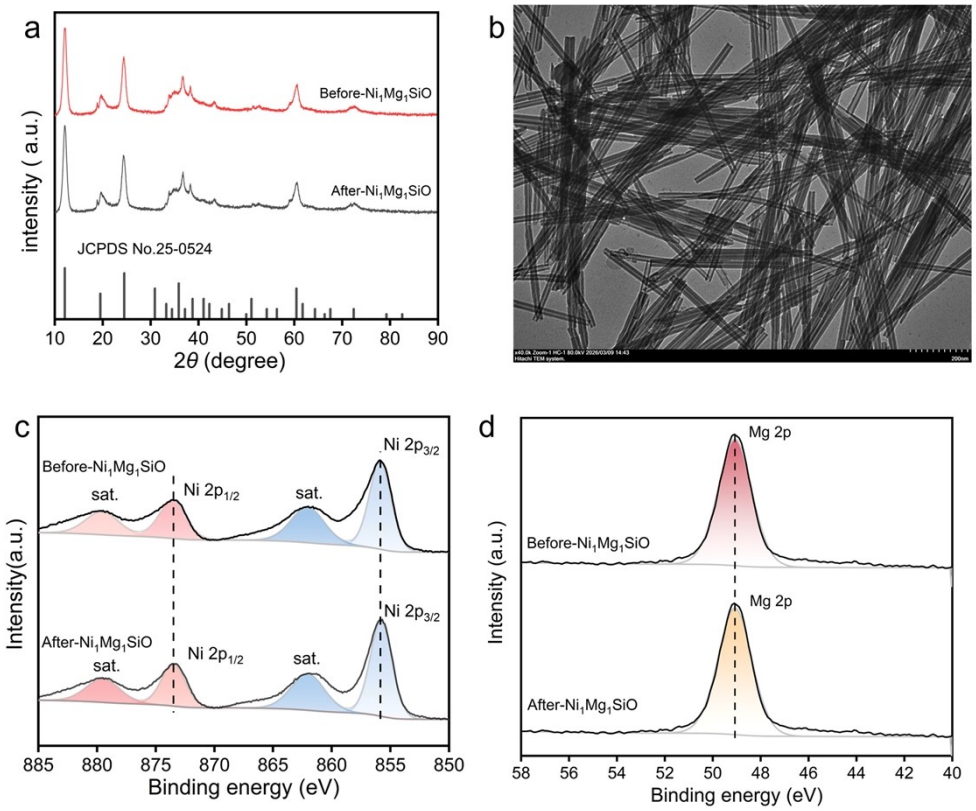

Fig. S25 XRD, TEM and XPS characterizations of Ni_1Mg_1SiO NTs before and after cycling test at −0.79 V vs. RHE in H-cell.

XRD, TEM and XPS were used to characterize the catalyst after the cycling catalysis. The XRD results indicated that there were no obvious changes in the phase structure (Fig. S25a). The TEM image also showed that the morphology remained unchanged (Fig. S25b). XPS further confirmed that the oxidation states of the main elements, Ni and Mg, did not change significantly (Figs. S25c and S25d). These findings clearly demonstrate that the Ni_1Mg_1SiO NTs catalyst exhibits exceptional stability and recyclability, thereby serving as an important reserve material for the electrocatalytic NO_2RR to synthesize NH_3.

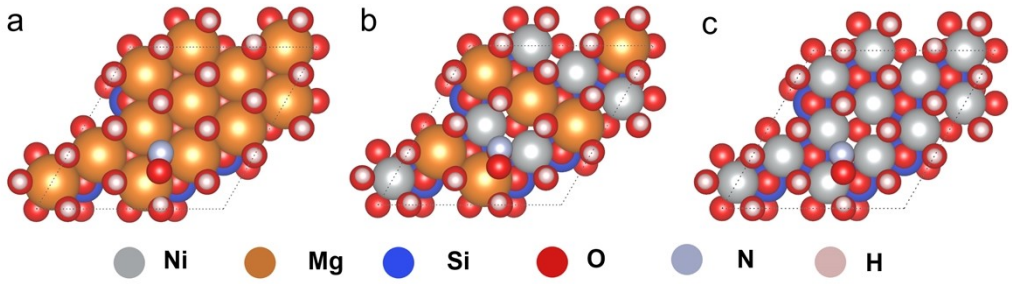

Fig. S26 Optimized structures for NO_2^- adsorption on slab models of (a) MgSiO NTs, (b) Ni_1Mg_1SiO NTs, and (c) NiSiO NPs, respectively.

Table S1 The detailed process of synthesizing $(Ni_x,Mg_{1-x})_3Si_2O_5(OH)_4$ products with different molar ratios of Ni^{2+} to Mg^{2+}.

Samples	Samples abbreviation	Molar ratios of Ni^{2+} to Mg^{2+}
$(Ni_{0.5},Mg_{0.5})_3Si_2O_5(OH)_4$	Ni_1Mg_1SiO	1 : 1
$(Ni_{0.25},Mg_{0.75})_3Si_2O_5(OH)_4$	Ni_1Mg_3SiO	1 : 3
$(Ni_{0.75},Mg_{0.25})_3Si_2O_5(OH)_4$	Ni_3Mg_1SiO	3 : 1
$Mg_3Si_2O_5(OH)_4$	MgSiO	0 : 1
$Ni_3Si_2O_5(OH)_4$	NiSiO	1 : 0

Table S2 Possibly existing oxygen-bridged multi-interface site units in different catalysts based on the systematic structural characterization results.

Catalysts	Oxygen-bridged multi-interface site units
NiSiO NPs	Ni-O-Ni、Ni-O-Si、Ni-O-Si-O-Ni
MgSiO NTs	Mg-O-Mg、Mg-O-Si、Mg-O-Si-O-Mg
Ni_1Mg_1SiO NTs	Ni-O-Ni、Ni-O-Si、Ni-O-Si-O-Ni Mg-O-Mg、Mg-O-Si、Mg-O-Si-O-Mg Ni-O-Mg、Ni-O-Si-O-Mg

Table S3 Comparison of NH_3 synthesis performances via electrocatalytic NO_2RR over Ni_1Mg_1SiO NTs with previously reported catalysts.

Catalysts	Electrolytes	NH_3 yield rates	FEs (NH_3)	*Ref.*
Ni_1Mg_1SiO NTs	**0.5 M Na_2SO_4 + 0.5 M $NaNO_2$**	**361.5 μmol h^{-1} cm^{-2} (or 6.15 mg h^{-1} cm^{-2})**	**96.4%**	***This Work***
$CoMoO_4$/NF	0.5 M Na_2SO_4 0.1 M $NaNO_2$	3.88 mg h^{-1} cm^{-2}	91.88 %	*Chem. Eng. J.*, **2024**, *498*, 155474.
$MoSe_{2-x}$/CC	0.1 M PBS 0.1 M $NaNO_2$	446.0 μmol h^{-1} cm^{-2}	96.9%	*Mater. Today Phys.*, **2023**, *36*,101170.
$OvTiO_2$-PdCu	0.5 M Na_2SO_4 0.1 M $NaNO_2$	366.4 μmol h^{-1} cm^{-2}	87.4%	*Small*, **2024**, *20*, 2403865.
V–TiO_2/TP	0.1 M NaOH 0.1 M $NaNO_2$	540.8 μmol h^{-1} cm^{-2}	93.2%	*Mater. Today Phys.*, **2023**, *30*, 100944.
Mo_1–ZrO_2	0.5 M Na_2SO_4 0.1 M $NaNO_2$	346.92 μmol h^{-1} cm^{-2}	94.83%	*J. Colloid Interf. Sci.*, **2024**, *653*, 390−395.
CoB@TiO_2/TP	0.1 M Na_2SO_4 (400 ppm $NaNO_2$)	233.1 μmol h^{-1} cm^{-2}	95.2%	*J. Cleaner Product.*, **2023**, *424*, −.
Pd_1/BN	0.5 M Na_2SO_4 0.1 M $NaNO_2$	347.1 μmol h^{-1} cm^{-2}	91.7%	*Inorg. Chem. Front.*, **2022**, *9*, 6075−6079.
FeP/PGP	1 M NaOH 0.1 M $NaNO_2$	354.92 μmol h^{-1} cm^{-2}	93.23 %	*Appl. Surf. Sci.*, **2025**, *713*, 164265.

Table S4 The concentrations of metal ions in the fresh electrolyte and after electrocatalysis by using Ni_1Mg_1SiO NTs as catalyst was detected by ICP.

Samples	Concentration of metal ions (ppm)	
	Ni^{2+}	Mg^{2+}
Fresh electrolyte	0.008474	0.008902
Electrolyte after electrocatalysis	0.008775	0.016456